IET Electric Power Applications

Review Article

IET Journals
The Institution of Engineering and Technology

Overview of fast on-board integrated battery chargers for electric vehicles based on multiphase machines and power electronics

ISSN 1751-8660
Received on 19th June 2015
Accepted on 24th August 2015
doi: 10.1049/iet-epa.2015.0292
www.ietdl.org

Ivan Subotic[1], Nandor Bodo[1], E. Levi[1] ✉, Boris Dumnic[2], Dragan Milicevic[2], Vladimir Katic[2]

[1]*School of Engineering, Technology and Maritime Operations, Liverpool John Moores University, Liverpool L3 3AF, UK*
[2]*Faculty of Technical Sciences, University of Novi Sad, 21000 Novi Sad, Republic of Serbia*
✉ *E-mail: e.levi@ljmu.ac.uk*

Abstract: The study provides an extensive overview of on-board integrated chargers for electric vehicles that are based on multiphase (more than three phases) machines and power electronics. A common attribute of all discussed topologies is that they do not require a charger as a separate device since its role is transferred to the already existing drivetrain elements, predominantly a multiphase machine and an inverter. The study demonstrates how additional degrees of freedom that exist in multiphase systems can be conveniently utilised to achieve torque-free charging operation. Therefore, although three-phase (or multiphase) currents flow through machines' stator windings, they do not generate any torque; thus the machines do not have to be mechanically locked. Cost and weight saving is achieved in this way, while the available space is increased. For each topology operating principles are explained, and its control elaborated in detail for both charging and vehicle-to-grid mode. Finally, the validity of theoretical considerations and control algorithms of some of the existing charging solutions is experimentally verified and experimental performance of all discussed topologies is compared.

1 Introduction

One of the main problems that hinder a wider spread of electric vehicles (EVs) is certainly battery charging. Typical concerns of potential customers are usually classified as the 'driving range anxiety': will they be able to find charging stations along their way, and will the charging process take too long? These two concerns come from the experience with internal combustion engine vehicles, where the re-fuelling (i.e. charging) process finishes in minutes and fuel stations are standardised and therefore widely spread. In what follows a short overview of battery charging options for EVs is given.

At present there are two main types of battery charging systems [1], namely off-board and on-board. In the former, the charger is placed outside the vehicle and provides a dc output on its terminals that are directly connected to an EV battery. Since it is not contributing to the vehicle weight, it can be very heavy. This allows it to be rated for high powers and thus capable of fully charging an EV battery within a few minutes. However, a limiting factor is the price, which measures in tens of thousands of dollars [2]. Therefore, number of these chargers is limited and they are not widely spread.

The second type are on-board chargers. They allow EVs to be charged directly from a single-phase (slow charging) or three-phase (fast charging) mains. As ac mains are widely available, this option does not demand expensive infrastructure, which is a clear advantage. They can be conductive, where the whole charger is placed on-board the vehicle, and inductive [3, 4], which require a part of the charger to be outside the vehicle. While on-board chargers perform the same function as off-board chargers, unlike them they have to be light and small to fit inside EVs. Although making a fast on-board charger is not a technological challenge, a charger like that would be too heavy and large to place on-board, and would significantly increase vehicle's cost. Therefore, at present, on-board chargers are usually capable only of slow charging [5].

One possible manner of significantly increasing the power of on-board chargers is their integration with existing power electronic components [6, 7]. A drivetrain that is required for propulsion and components that are required for charging purposes have great similarity. To be precise, inverter which is required for propulsion mode can as well operate in rectification mode. To accomplish rectification, it only requires an input filter. On the other hand, machine consists of windings, which can take on the role of the filter. Therefore, since propulsion and charging are never happening at the same time, it is possible to use the same drivetrain for both functions. By doing so, additional weight and cost are not introduced to the system. Charging power is then only limited by the power rating of the propulsion components; thus, theoretically, high charging powers could be achieved. The need for expensive charging infrastructure is eliminated in this way, and fast charging can be achieved, all without an increase of the vehicle cost, weight or required space.

However, the realisation of integrated chargers is not straightforward, especially for a fast charging process (i.e. charging from a three-phase grid). Problems are mainly associated with torque production in the machine during the charging process [8–11]. Namely, if a machine is used as an input filter, three-phase currents flow through the machine windings during the fast charging process. In three-phase induction machine (IM) torque will result, which will try to bring the machine into rotation while in a permanent magnet (PM) synchronous machine mechanical vibrations, acoustic noise and accelerated aging will result. This also significantly worsens the efficiency, as substantial amount of energy is wasted. Therefore, direct integration of a three-phase machine into fast charging process is not an option, unless special solutions are resorted to.

These problems do not exist if the charging is from single-phase mains, as single-phase current cannot produce a starting torque in a machine. This is the main reason behind the fact that the majority of integrated charging solutions are proposed for single-phase charging. In what follows only integrated fast chargers employing IM and PM machines are considered, as these are the most common types of propulsion machines that can be found in commercial EVs [12].

In [13] the torque production is avoided by utilising a synchronous machine with an excitation winding. For the charging process rotor power supply has to be cut off to prevent torque production. Stator

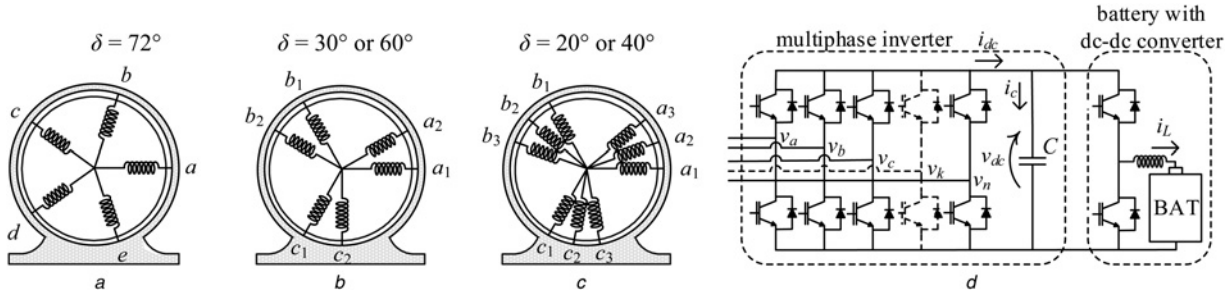

Fig. 1 *Elements of a multiphase powertrain*

a Five-phase machine (δ represents the angle between the first two phases)
b Six-phase machine (shown with a single neutral point)
c Nine-phase machine (shown with a single neutral point)
d Rest of the drivetrain consisting of an *n*-phase inverter (*n* equals the number of machine phases) and a battery (with or without a dc-dc converter)

winding has to be reconfigured from star connection into an open-end topology to allow a connection to the three-phase mains. Although a torque is not produced during the charging process, the main disadvantages are the requirement of hardware reconfiguration between the propulsion and the charging mode and the need for a wound rotor and excitation winding supply, which increase the cost of the system.

Another solution that does not cause torque production is 'Chameleon' charger [14]. It presents the first integrated fast charger that is commercially used in industry. It is currently on-board Renault ZOE, and it appears to be relying on patents [15, 16]. However, a non-integrated rectifier is required. Upon rectification, a synchronous machine with excitation winding performs a function of filtering inductances since dc current is passed through it. Advantages of the solution are that a torque is not produced in the machine and that there is no need for hardware reconfiguration between the operating modes. The downside is a requirement for non-integrated elements.

An interesting integrated charging solution for drives powered by two separate power sources is presented in [17]. By adding a single non-integrated on-board charger, charging of both sources can be accomplished. While the first battery is charged from the charger in a conventional manner, the second is charged from the first through a three-phase machine in an open-end winding configuration. An obvious drawback is that a non-integrated charger is required.

Integrated topologies utilising multiple propulsion motors are considered in [18, 19]. They do not require hardware reconfiguration, and there is no torque production in machines during the fast charging process. However, the cost of such a system would be considerably higher compared with drivetrains with a single machine, which is the standard option in EVs.

Finally, a solution that does not require non-integrated elements and utilises a single machine is presented in [20, 21]. Mid-points of the machine windings are made accessible so that grid terminals can be attached to them. By assuring that the same currents flow in each pair of half-windings in spatial opposition, zero torque production is achieved. A hardware reconfiguration is not required. However, a three-phase machine with accessible mid-points has to be custom-made and is in essence a symmetrical six-phase (a multiphase) machine in the charging mode. A similar solution, based on a six-phase machine, which requires a hardware reconfiguration is presented in [22].

It is obvious that a standard three-phase IM and PM machines cannot be conveniently integrated into a three-phase charging process, without torque production in them or without a requirement for non-integrated elements. However, this is not the case if multiphase (more than three phases) machines are utilised.

Multiphase systems have additional degrees of freedom compared with those with three phases. As it will be shown in the paper, these degrees of freedom can be utilised to achieve torque-free integrated charging process. This makes multiphase machines particularly suitable for EV charging applications. The paper provides an overview of recently introduced integrated charging solutions employing multiphase machines, and is organised as follows. In Section 2 integrated multiphase charging topologies are presented and their operating principles explained. A principle of phase transposition is elaborated. Control algorithms of all considered topologies are detailed and discussed in Section 3. Finally, experimental performance of the integrated topologies is assessed using selected experimental results in Section 4. Section 5 concludes the paper.

2 Topologies and operating principles

Multiphase machines possess more than three phases. Typical multiphase machines with phase numbers equal to 5, 6 and 9 are shown in Figs. 1*a*–*c*, respectively. If spatial angles between any two consecutive machine phases are the same, the machine is called symmetrical. On the other hand, if phases are spatially shifted by different angles (as in Figs. 1*b* and *c*), a machine is asymmetrical. Multiphase machines can have one or multiple isolated neutral points. Although in Fig. 1, for easier representation, they are all shown as having a single neutral point, it is typical that six-phase machines have two, while nine-phase machines have three isolated neutral points in propulsion mode of operation. Finally, multiphase machines are commonly supplied from a multiphase inverter, which is shown in Fig. 1*d* together with a battery and an optional bidirectional dc–dc converter, which may or may not exist; however this is irrelevant for further considerations.

Integrated chargers based on multiphase machines are considered in [23–28]. They can be separated into two categories: one employs a three-phase grid [23–25], while the other takes in supply from a multiphase voltage source [26–28]. These two groups are analysed independently in what follows.

Probably the most important aspect of the analysis is whether a torque is produced in machines during the charging process, and a special attention is paid to this issue. The analysis requires observation of the system in a decoupled domain. However, decoupling transformation of multiphase systems significantly differs and is more complex than the one used for three-phase systems. Therefore, before proceeding to the two groups of topologies, the essence of multiphase decoupling transformations is revisited.

2.1 Multiphase system decoupling transformation

The well-known Clarke's decoupling transformation for a three-phase system is only a special case of the corresponding transformation for a general *n*-phase symmetrical configuration, in which two consecutive phases are spatially shifted by $2\pi/n$. The full transformation matrix is available in [29] and it applies to all symmetrical multiphase systems, with both an odd and an even number of phases, as long as there is a single neutral point. If a multiphase system has more than one neutral point, as the case

IET Electr. Power Appl., 2016, Vol. 10, Iss. 3, pp. 217–229

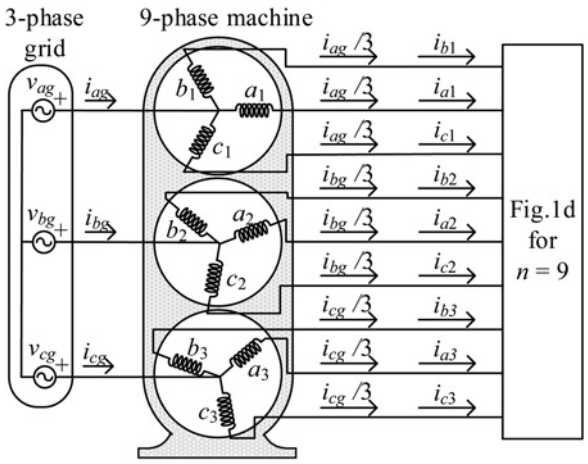

Fig. 2 *Integrated charging topology based on a nine-phase machine [23]*

typically is with n-phase configurations composed of k three-phase windings (i.e. $n = 3k$), the transformation matrix changes.

In general, given an n-phase symmetrical topology with a single neutral point, the decoupling transformation leads to the system representation in INT[$(n-1)/2$] mutually orthogonal planes plus one (two) zero-sequence components when n is an odd (even) number, respectively. Since the transformed model possesses two components in each of the $(n-1)/2$ planes, it is possible to replace each pair of real quantities with a single complex number. Such a complex number is a two-dimensional space vector in the given plane.

In a symmetrical multiphase system with k isolated neutral points, the number of orthogonal planes reduces and becomes equal to $(n-k)/2$. The number of zero-sequence components increases correspondingly and becomes equal to k. Hence the last k rows (rather than just the last row or the last pair of rows, for the single neutral point and an odd, respectively even, phase number) now represent zero-sequence components.

When a multiphase system is designed with k multiple three-phase windings, in addition to the symmetrical topology there exists a possibility of creating an asymmetrical topology (in a sense of the distribution of the magnetic axes of the individual phase windings), in which spatial displacement between phases a of consecutive three-phase windings is π/n. Decoupling transformation for such an n-phase topology is most easily determined by regarding the topology as a semi $2n$-system and taking as the starting point the Clarke's transformation matrix for a $2n$-phase system. The resulting matrix for an asymmetrical n-phase system differs substantially from the corresponding one for a symmetrical n-phase system (see e.g. [23, 29] where the matrix is given for asymmetrical nine- and six-phase systems, respectively). Regarding the zero-sequence components, the same remarks apply for a system with k isolated neutral points as for a symmetrical system with the same number of three-phase windings.

Regardless of the phase number and independent of the system nature (symmetrical or asymmetrical), the electromechanical energy conversion is always restricted to the first plane (α–β) as long as the machine is with near-sinusoidal magneto-motive force. Hence the components in all the other planes, in which the components are further on labelled as x–y components, appear as additional degrees of freedom that do not exist in a three-phase system. It is this feature of multiphase systems that makes them exceptionally well-suited for realisation of integrated on-board battery chargers, as discussed further on in the paper. In simple terms, it becomes possible to divert the excitation from the first (torque producing) plane into other planes where components do not yield torque production. Depending on the actual topology, it is possible to either completely divert the excitation from the α–β plane into an x–y plane, in which case there is no mutual flux and torque production at all, or it is possible to divert part of the excitation, so that only pulsating field (which cannot cause torque at standstill) is created in the α–β plane. Which planes are excited in charging topologies of [23–28] and how is discussed next.

2.2 Charging from a three-phase grid

Topologies of [23–25] enable charging from a three-phase grid, and they are shown in Figs. 2–3. The right-hand side parts of figures consist of the circuit that is given with Fig. 1*d* (for the respective number of phases n).

From Figs. 2–3 it can be seen that in each topology three-phase grid currents flow through windings of a multiphase machine. To comply with grid standards and regulations, grid currents have to be near-sinusoidal, that is

$$i_{kg} = \sqrt{2}I\cos(\omega t - l2\pi/3) \quad l = 0, 1, 2 \quad k = a, b, c \qquad (1)$$

It follows from Figs. 2–3 that some converter legs are connected to the same grid phase (e.g. in Fig. 2 converter legs a_1, b_1, and c_1 are all connected to a single grid phase, ag). All converter legs connected to a common grid phase are controlled with the same modulation signals. This means that the same currents flow through these phases. It should be noted that in practice certain inequalities in currents may appear since phase impedances may not be perfectly

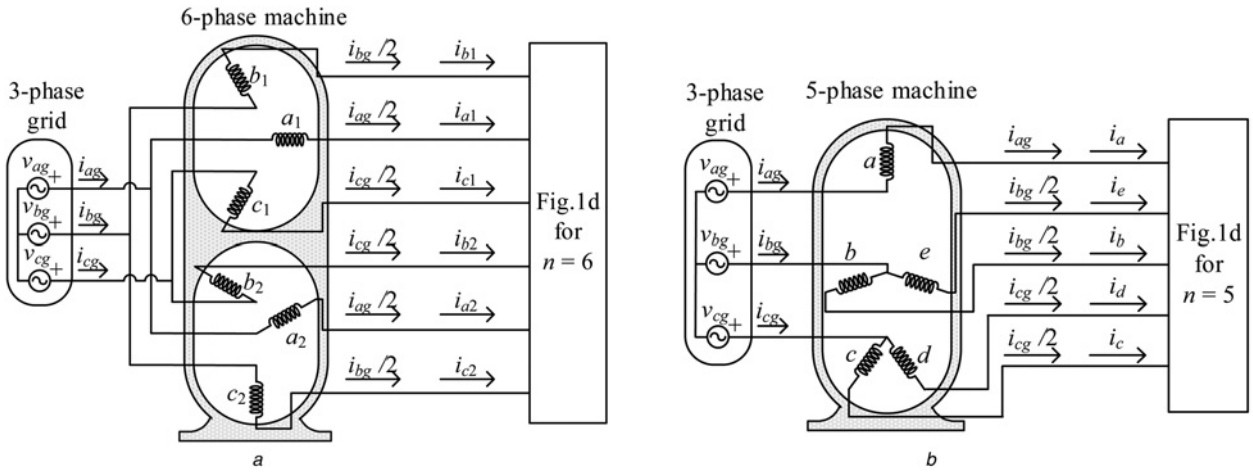

Fig. 3 *Integrated charging topologies based on*

a Asymmetrical six-phase machine [24]
b Five-phase machine [25]

Table 1 Correlations between machines' and grid currents

Topology	Correlations
Fig. 2	$i_{a1} = i_{b1} = i_{c1} = i_{ag}/3 \quad i_{a2} = i_{b2} = i_{c2} = i_{bg}/3 \quad i_{a3} = i_{b3} = i_{c3} = i_{cg}/3$
Fig. 3*a*	$i_{a1} = i_{a2} = i_{ag}/2 \quad i_{b1} = i_{c2} = i_{bg}/2 \quad i_{c1} = i_{b2} = i_{cg}/2$
Fig. 3*b*	$i_a = i_{ag} \quad i_b = i_e = i_{bg}/2 \quad i_c = i_d = i_{cg}/2$

identical in all machine phases, so that a proper balancing technique has to be employed. This is however beyond the scope of the paper, and, in what follows, a perfect sharing among hard-paralleled machine phases is assumed.

By inspection of Figs. 2–3 it can be seen that the relationship between machine and grid currents is as summarised in Table 1. Considering that grid phase currents are fixed and given with (1), machines' behaviour is completely determined by Table 1. As elaborated in the previous section, torque analysis requires observation of machines' currents in decoupled domain. For this purpose, multiphase decoupling matrices have to be applied to machine currents. As machines' neutral points are connected through the grid, the matrices take the form valid for the case with a single neutral point. Decoupling matrices for five-, six- and nine-phase systems can be found in [23–25].

When corresponding decoupling matrices are applied to machines' currents given in Table 1 (by taking into account (1)), current components listed in Table 2 are obtained. Derivation procedure for these equations is given in the Appendix 1. In Table 2 current components of each two axes belonging to the same plane are represented together as a single expression in a two-dimensional space vector form.

For easier analysis the expressions are plotted using Matlab and the results are shown in Fig. 4 for $I = 1$ pu. From Fig. 4*a* it can be seen that in the case of the asymmetrical nine-phase machine the excitation is completely transferred from torque-producing (α–β) plane into x_1–y_1 plane, which is not capable of torque production. Therefore a torque cannot be produced during the charging process. The nine-phase machine has two more passive planes (x_2–y_2 and x_3–y_3) which are, as is obvious from Fig. 4*a*, without excitation.

In the case of an asymmetrical six-phase machine and a five-phase machine only a part of the excitation is transferred from torque-producing (α–β) into a non-torque producing (x–y) plane (Figs. 4*b* and *c*). However, as can be seen, the excitation in the first (α–β) plane is only pulsating. Therefore, as explained in the previous section, it cannot produce a starting torque.

It can be concluded that topologies from this section do not have to be mechanically locked as a torque is not produced in them during the charging process. Therefore, the machines can be used as a simple set of passive filtering components (inductances and resistances).

2.3 Charging from a multiphase voltage source

Integrated chargers, described in [26–28], utilise a multiphase voltage source, and their topologies are shown in Figs. 5 and 6. Topologies given in Figs. 5*a*, 5*b* and 6 utilise an asymmetrical

Table 2 Excitation mapping into machines' planes

Topology	Excitation in the torque producing plane	Excitation in the non-torque producing (x–y) plane(s)
Fig. 2	$\underline{i}_{\alpha\beta} = 0$	$\underline{i}_{x1y1} = I\{(2/3)\cos(\omega t) + (1/\sqrt{3})\sin(\omega t) - j(1/\sqrt{3})\cos(\omega t)\}$
		$\underline{i}_{x2y2} = 0$
		$\underline{i}_{x3y3} = 0$
Fig. 3*a*	$\underline{i}_{\alpha\beta} = \sqrt{3/2}I\cos(\omega t - \pi/12)\cdot(0.966 + j\cdot 0.259)$	$\underline{i}_{xy} = \sqrt{3/2}I\cos(\omega t + 5\pi/12)\cdot(0.259 + j0.966)$
Fig. 3*b*	$\underline{i}_{\alpha\beta} = I\cdot\sqrt{2}\cos(\omega t - 0.659)$	$\underline{i}_{xy} = I\cdot\sqrt{2}\cos(\omega t + 0.659)$

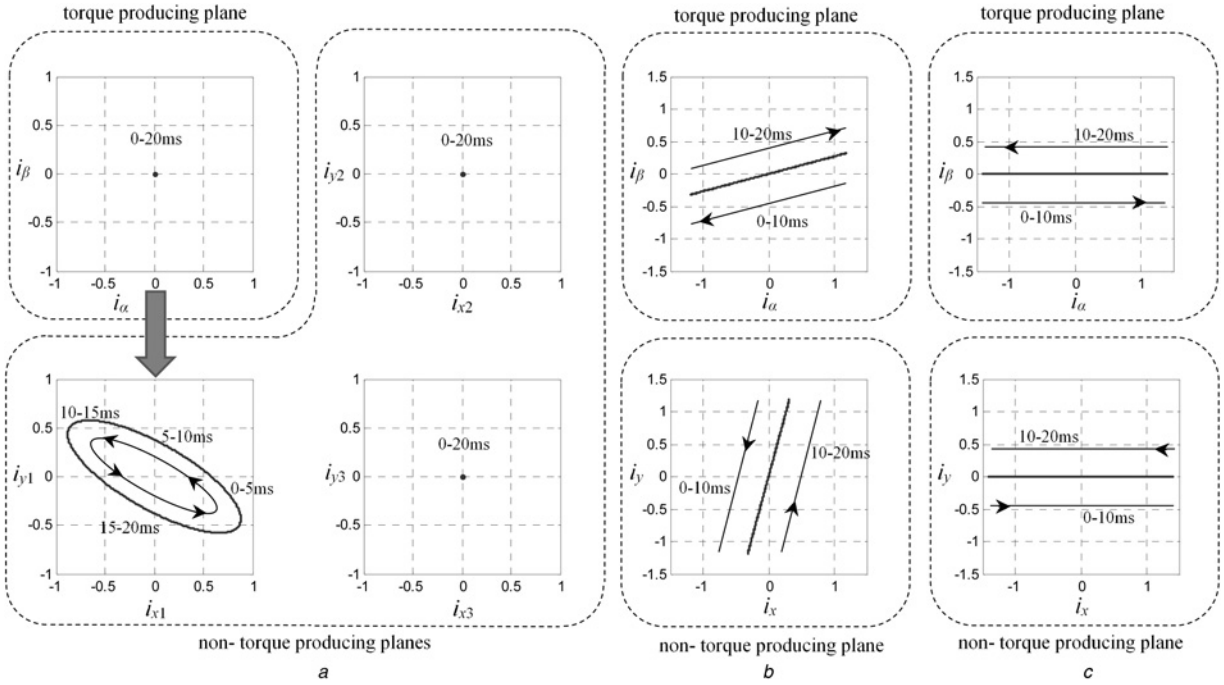

Fig. 4 *Graphical representation of equations given in Table 2 for the topologies shown in*

a Fig. 2
b Fig. 3*a*
c Fig. 3*b*

IET Electr. Power Appl., 2016, Vol. 10, Iss. 3, pp. 217–229

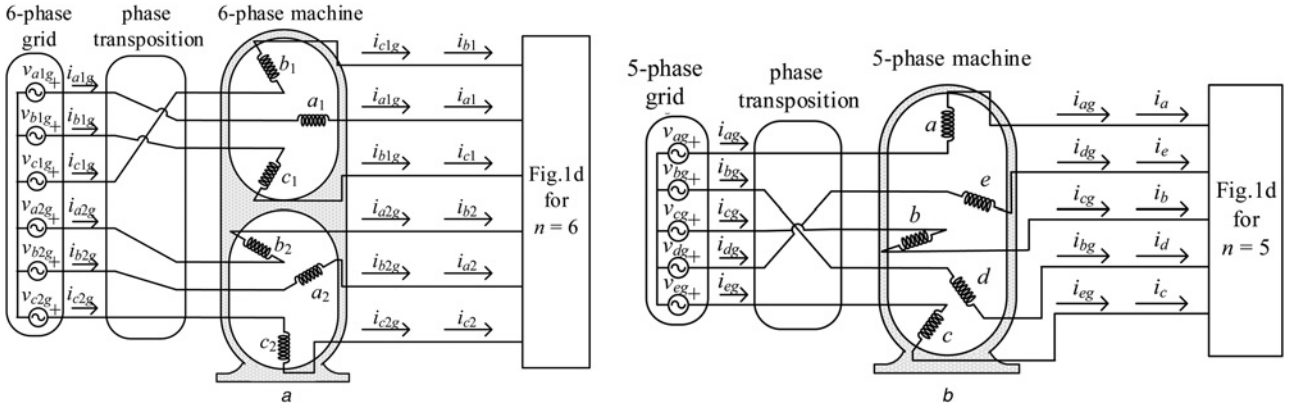

Fig. 5 *Integrated charging topologies supplied from a multiphase voltage source and based on*

a An asymmetrical six-phase machine [26]
b A five-phase machine [27]

six-phase [26], a five-phase [27], and a symmetrical six-phase voltage source [28], respectively. In [30] it is shown how isolated asymmetrical and symmetrical six-phase voltage source can be provided by means of an off-board transformer with dual secondary winding; this is however beyond the scope here.

To have a charging process with a unity power factor, the currents of multiphase voltage sources of Figs. 5*a*, *b* and 6 have to be given with

$$\begin{aligned} i_{k_1\mathrm{g}} &= \sqrt{2}I\cos(\omega t - l\pi/6) \quad l = 0, 4, 8 \quad k = a, b, c \\ i_{k_2\mathrm{g}} &= \sqrt{2}I\cos(\omega t - l\pi/6) \quad l = 1, 5, 9 \quad k = a, b, c \end{aligned} \tag{2}$$

$$i_{k\mathrm{g}} = \sqrt{2}I\cos(\omega t - l2\pi/5) \quad l = 0, 1\ldots4 \quad k = a, b, c, d, e \tag{3}$$

$$\begin{aligned} i_{k\mathrm{g}} &= \sqrt{2}I\cos(\omega t - l\pi/3) \quad l = 0, 1\ldots5 \\ k &= a_1, a_2, b_1\ldots c_2 \end{aligned} \tag{4}$$

respectively.

As can be seen from Fig. 5, phases of a multiphase voltage source are not connected to the machine phases following the natural order (i.e. phases $a_{1\mathrm{g}}$–$c_{2\mathrm{g}}$ of the grid to the machine phase a_1–c_2, respectively). Instead, they are connected based on the principle of phase transposition, which aims to transfer the excitation from a torque-producing (α–β) into a non-torque producing plane(s). The theory of the required connections is developed in [31] and is respected in topologies of Fig. 5. The topology in Fig. 6 utilises a modified version of phase transposition. It aims to transfer only a part of the excitation from the torque-producing into a non-torque producing plane, again leaving the machine without an average torque production.

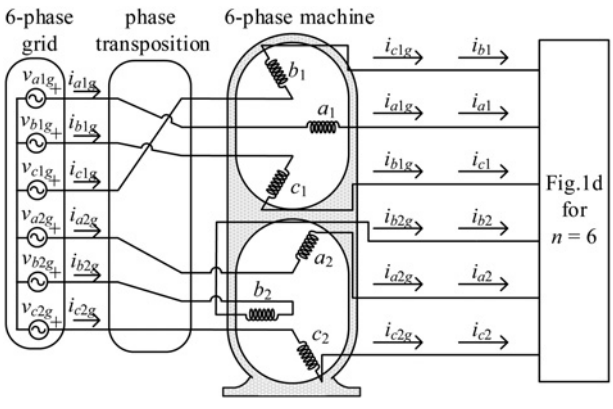

Fig. 6 *Integrated charging topology supplied from a multiphase voltage source and based on a symmetrical six-phase machine [28]*

By observing Figs. 5 and 6, the correlations between machine currents and currents of a multiphase voltage source (for convenience called 'grid currents') can be made. These are given in Table 3.

Similarly as in the previous section, multiphase system decoupling transformations can be utilised to perform analysis of torque production in the machines. After applying decoupling transformations onto currents in Table 3 (by utilising (2)–(4)), the equations given in Table 4 are obtained. The principles of derivations in Appendix 1 still apply.

To allow easier analysis, expressions are again represented graphically, Fig. 7. In Fig. 7*a*, which applies to all topologies but with different values and is shown for a six-phase topology, grid current components are given. They are, as can be seen, only in the first plane. However, from Figs. 7*b* and *c* it can be seen that the excitation in the asymmetrical six-phase and the five-phase machine is completely transferred from the first (torque-producing) into the second plane, thanks to the phase transposition. Similarly as in Fig. 4*a*, the first plane is left without any excitation.

In the case of a symmetrical six-phase machine, only a part of the excitation is transferred into the second plane (Fig. 7*d*). However, similarly as in Figs. 4*b* and *c*, the remaining excitation in the first plane pulsates in a single direction, and therefore cannot produce a starting torque.

It is clear that not just in the case of topologies supplied from a three-phase grid (Figs. 2–3), but also in those supplied from a multiphase voltage source (Figs. 5–6) a torque cannot be produced during the charging process. Therefore, in all topologies the

Table 3 Correlations between machines' and grid currents

Topology	Correlation between machine and grid currents
Fig. 5*a*	$i_{a1} = i_{a1\mathrm{g}}$ $i_{b1} = i_{c1\mathrm{g}}$ $i_{c1} = i_{b1\mathrm{g}}$ $i_{a2} = i_{b2\mathrm{g}}$ $i_{b2} = i_{a2\mathrm{g}}$ $i_{c2} = i_{c2\mathrm{g}}$
Fig. 5*b*	$i_a = i_{ag}$ $i_b = i_{cg}$ $i_c = i_{eg}$ $i_d = i_{bg}$ $i_e = i_{dg}$
Fig. 6	$i_{a1} = i_{a1\mathrm{g}}$ $i_{b1} = i_{c1\mathrm{g}}$ $i_{c1} = i_{b1\mathrm{g}}$ $i_{a2} = i_{a2\mathrm{g}}$ $i_{b2} = i_{b2\mathrm{g}}$ $i_{c2} = i_{c2\mathrm{g}}$

Table 4 Excitation mapping into machines' planes

Topology	Excitation in torque producing plane	Excitation in non-torque producing plane
Fig. 5*a*	$\underline{i}_{\alpha\beta} = 0$	$\underline{i}_{xy} = \sqrt{6}I\exp(\mathrm{j}\omega t)$
Fig. 5*b*	$\underline{i}_{\alpha\beta} = 0$	$\underline{i}_{xy} = \sqrt{5}I\exp(\mathrm{j}\omega t)$
Fig. 6	$\underline{i}_{\alpha\beta} = \sqrt{6}I\cos(\omega t)$	$\underline{i}_{xy} = \mathrm{j}\sqrt{6}I\sin(\omega t)$

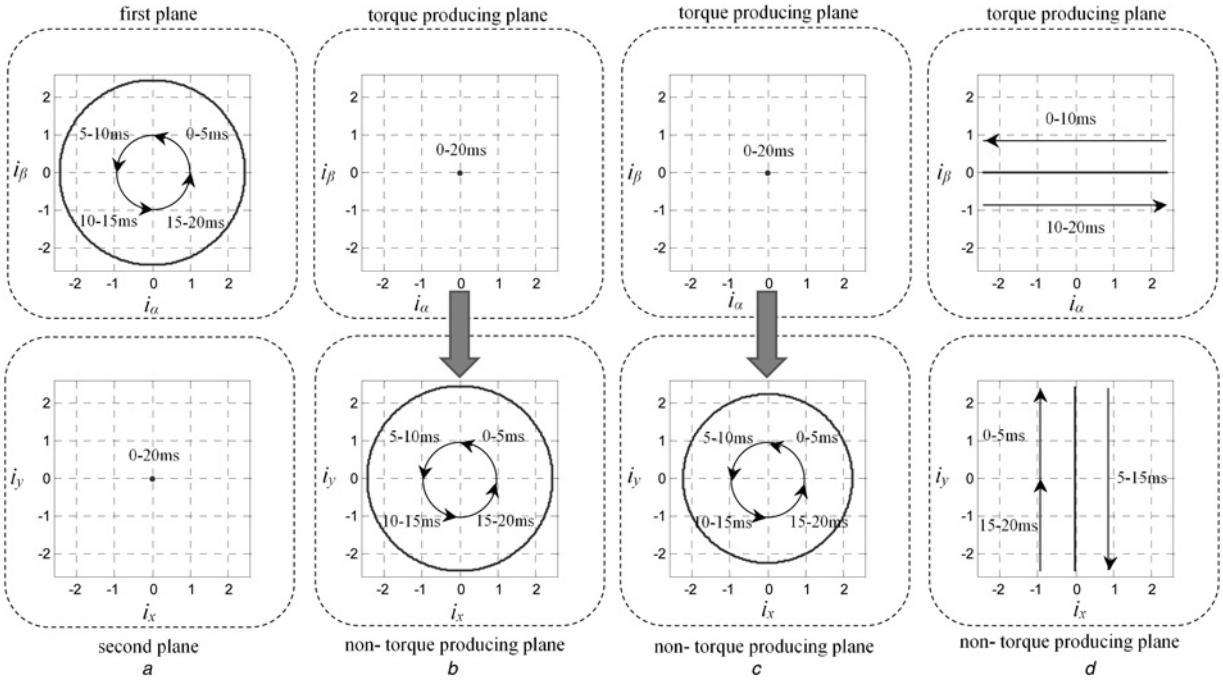

Fig. 7 *Behaviour of solutions with multiphase voltage supply*

a Excitation mapping of a multiphase voltage supply discussed in Section 2.3
b Graphical representation of equations given in Table 4 for the topology shown in Fig. 5*a*
c Graphical representation of equations given in Table 4 for the topology shown in Fig. 5*b*
d Graphical representation of equations given in Table 4 for the topology shown in Fig. 6

machine can be considered as a set of passive components. This facilitates equivalent circuit representation and the control of the topologies, which is discussed in the next section.

3 Control algorithms

3.1 Charging from a three-phase grid (Figs. 2–3)

As machines in all considered charging topologies act as pure passive components, their equivalent circuits are to a large extent simplified. For topologies in Figs. 2–3 the equivalent circuit is given in Fig. 8. As can be seen it is a simple three-phase power factor correction (PFC) rectifier. This section considers its control.

As already noted, to comply with grid regulations, grid currents have to be given (approximately) with (1) and to be in phase with grid voltages. The voltage oriented control is commonly utilised for the purpose. Its scheme is well known and it is shown in Fig. 9.

The process initiates by gathering information on dc-bus voltage and grid voltages and currents. Additional current sensors for grid currents are not required as in all topologies they can be obtained from machine currents (Table 1). From grid voltage measurements voltage angular position can be obtained by means of a phase-locked loop (PLL). This information is then utilised to transform grid currents into a reference frame that is in phase with the grid voltage. The transformation is necessary to separate the grid current component that is in phase with the voltage (i_{dg}) from the one that is shifted by 90° from it (i_{qg}). It consists of a three-phase decoupling transformation and a subsequent rotational transformation. These two are lumped together in Fig. 9 under the name 'coordinate transformation'. To obtain a unity power factor only the grid current component that is in phase with the voltage (i_{dg}) can have non-zero values, while the other one (i_{qg}) should be suppressed by the control.

There are two ways of obtaining the reference for the current component that is in phase with the grid voltage, and they are dependent on the battery state of charge. At the beginning of the charging process the battery should be charged by a uniform maximum allowed current (commonly known as constant current, that is, CC, mode) [32]. In this mode the reference for the grid current component i_{dg} does not change much. However, instead of having it as a constant it can be obtained as the output of a PI controller of the battery charging current i_L. This decreases

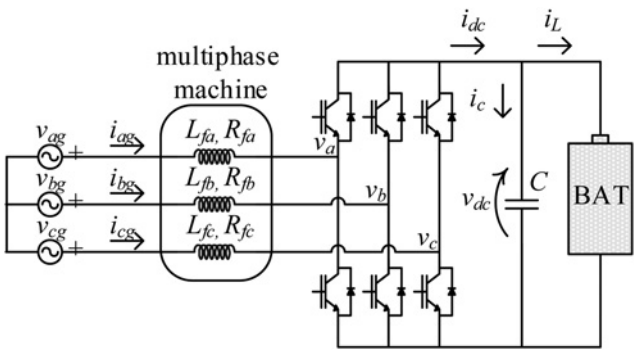

Fig. 8 *Equivalent scheme of integrated chargers utilising a three-phase grid (Figs. 2 and 3)*

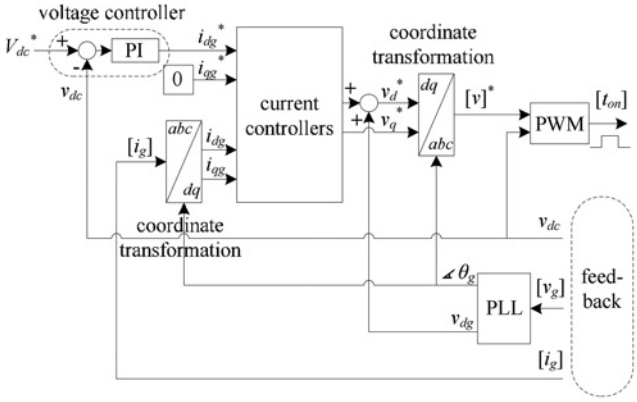

Fig. 9 *Control algorithm of the circuit in Fig. 8*

IET Electr. Power Appl., 2016, Vol. 10, Iss. 3, pp. 217–229

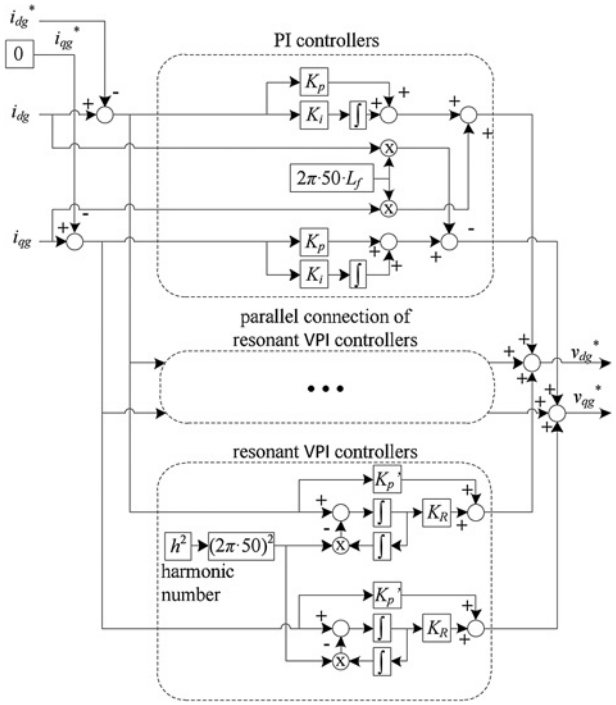

Fig. 10 '*Current controllers*' *block of Fig. 9*

charging power dependence on grid voltage fluctuations. The CC mode terminates when battery voltage reaches certain cut-off level. From that point, the battery has to be charged by a constant voltage (CV mode). In this mode the reference for the grid current component i_{dg} is obtained from a dc-bus voltage controller (Fig. 9). The charging process ends when the current drops to 10% of its maximum value.

After obtaining a reference for grid current component i_{dg} (in one of the two ways described in the previous paragraph), current control takes place inside the block 'current controllers' (Fig. 9). This block is shown in detail in Fig. 10. As both i_{dg} and i_{qg} are dc quantities they can be controlled to their references with PI controllers. In Fig. 10 the reference currents are subtracted from the real currents. The reverse sign comes from the fact that when the converter voltage increases the charging power decreases, and vice versa.

As inverter dead-time introduces low-order harmonics in the system, they have to be zeroed as well. The dominant harmonics are the −5, 7, −11 and 13th (as seen from a stationary reference frame). In the reference frame that rotates at a synchronous speed (in which the control is performed) they are seen as the −6, 6, −12 and 12th. As shown in [23, 25] they can be conveniently controlled by only two resonant vector proportional-integral (VPI) controllers at each of the two axes. Therefore, in Fig. 10 two pairs of resonant VPI controllers should be placed in parallel. They should be tuned at the 6 and 12th harmonic ($h = 6$ and $h = 12$). However, topologies in Figs. 3*a* and *b* require addition of further controllers, since those already described do not suffice. This presents the main control difference between topologies of Figs. 2 and 3, and the reason is discussed in what follows.

As can be seen from Fig. 8, the machine is represented as a set of three filter impedances. In the case of a nine-phase machine (Fig. 2) these are given with

$$R_{af} = R_{bf} = R_{cf} = R_s/3; \quad L_{af} = L_{bf} = L_{cf} = L_{\gamma s}/3 \tag{5}$$

where R_s and $L_{\gamma s}$ are machine's stator resistance and leakage inductance, respectively. The values are divided by three as the filter represents a parallel connection of three machine phases.

On the other hand, in topologies of Fig. 3 a pulsating field is produced in the rotor (Figs. 4*b* and *c*). As rotor now influences the charging process, the values of filter parameters are not only dependent on the stator but also on the rotor parameters. However, as explained in detail in [25], the rotor influence is higher on stator phases that are closer (spatially shifted by a smaller angle) to the direction of the field pulsation. As some machine phases are more and some less dependent on rotor parameters, the parameters of the equivalent scheme of the machine are not equal during the charging process. Naturally, the direct consequence are unequal values of filter parameters. Thus, for the topologies in Fig. 3 the following applies

$$R_{af} \neq R_{bf} \neq R_{cf}; \quad L_{af} \neq L_{bf} \neq L_{cf} \tag{6}$$

Unbalance in filter parameters is clearly present. It manifests primarily through grid current fundamental component that rotates at synchronous speed but in anti-synchronous (opposite) direction. Therefore, topologies in Figs. 3*a* and *b* require additional controllers to suppress it. This can be done by a pair of resonant VPI controllers tuned at the 2nd harmonic, placed in parallel with the existing controllers (under the block 'parallel connection of resonant VPI controllers'). For easier understanding, the current control techniques discussed in this section are summarised in Table 5.

Finally, the output of 'current controllers' block are voltage references for the converter. However they are in a rotational reference frame. To obtain references for phase voltages an inverse rotational and inverse decoupling transformation have to be applied. Finally, the signals enter the last block, which is a PWM unit. Carrier-based PWM with zero-sequence injection is used as a modulation strategy in subsequent experimentation.

3.2 Charging from a multiphase voltage source (Figs. 5–6)

Equivalent scheme of the topology in Fig. 5*b* is presented in Fig. 11*a*, while for the topologies of Figs. 5*a* and 6 it is given in Fig. 11*b*. It can be seen that in both cases it involves a multiphase PFC rectifier. Its control algorithm is given in Fig. 12. A great similarity with the one in Fig. 9 is obvious. However, there are four important differences which are discussed in what follows.

At first, information on more than three grid voltages enter the PLL block. Therefore, a decoupling transformation that is common at the start of the PLL algorithm [33] has to have a multiphase form: five-phase for the topology in Fig. 5*b*, and asymmetrical and symmetrical six-phase for topologies in Figs. 5*a* and 6, respectively. Once α and β components are obtained in this manner, the remaining part of the PLL algorithm can be used unaltered.

The second difference is in the PWM block, as it also has more than three inputs. The zero-sequence injection now differs from the one for three-phase systems, and its principles can be found in [34].

Table 5 Summary of current control structure for the topologies supplied from a three-phase grid

	Without rotor field (Fig. 2)	With pulsating field in the rotor (Figs. 3*a* and *b*)
Balanced system (equal per-phase filter parameters)	yes	no
Dead-time harmonics that map into the α–β plane	−5, 7, −11 and 13th	−5, 7, −11 and 13th
Number of PI controller pairs	single controller pair	single controller pair
Number of resonant VPI controller pairs in the α-β plane and their tuning (h)	two controller pairs $h = 6$, 12	three controller pairs $h = 2$, 6 and 12

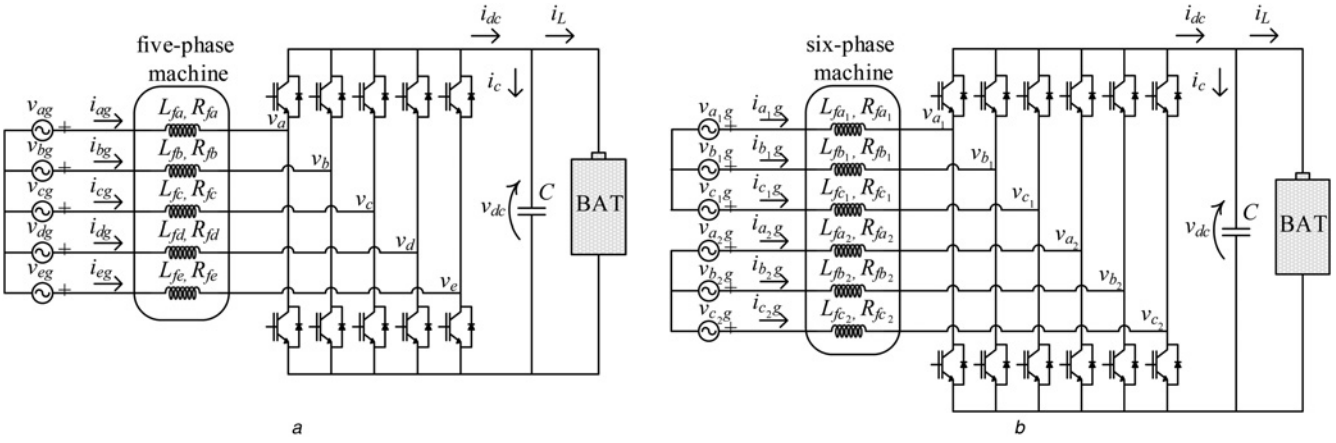

Fig. 11 *Equivalent scheme of integrated chargers utilising*

a Five-phase voltage source (Fig. 5*b*)
b Asymmetrical and symmetrical six-phase voltage source (Fig. 5*a* and 6)

As there are more than three grid currents, the block 'coordinate transformation' must have a multiphase form. It should be noted that notations '*abc*' and '*dq*' are used only to signify a phase and a rotational domain, respectively, and do not refer to a three-phase system. The decoupling transformation should have a five-phase form for the topology in Fig. 5*b*, and asymmetrical and symmetrical six-phase form for topologies in Figs. 5*a* and 6, respectively. There are now five or six inputs to a subsequent rotational transformation. The manner of transformation of α–β components remains the same, while for x–y components a somewhat different rotational transformation should be applied, as discussed shortly.

The final difference between a three-phase and a multiphase PFC rectifier is in the block 'current controllers'. From Fig. 12 it follows that there are now four current components that enter this block and that require control. The block is shown separately in Fig. 13. It can be seen that the control of α and β components remains the same as for the three-phase PFC rectifier (Fig. 10). From Fig. 7*d* it can be seen that the topology in Fig. 6 has a pulsating field production in the rotor. Therefore, its equivalent scheme filter parameters are unequal, the reason being the same as for the topologies in Fig. 3. Again, the same control as in Fig. 10 can suppress the unbalance. On the other hand, topologies of Fig. 5 do not have excitation in the first plane. Therefore, as for the topology in Fig. 2, they have equal filter parameters of the equivalent scheme and do not require additional control of unbalance. Therefore, both fundamental and low-order harmonics that map into the first plane are controlled as in Fig. 10.

However, some of the dead-time induced low-order harmonics map into the second (x–y) plane, and therefore they cannot be seen or controlled from the α–β plane. In the asymmetrical six-phase case (Fig. 5*a*), these are the 5 and –7th. In [30] it is shown that these can be controlled from the second (x–y) plane in a similar manner as low-order harmonics in the first plane are controlled. However, for this, the x–y plane should also rotate, but in anti-synchronous direction. Therefore, as already noted, the rotational transformation in the block 'coordinate transformation' (Fig. 12) should also transform x–y components. In the particular case of the asymmetrical six-phase system, the rotation of the x–y plane should be at synchronous speed in anti-synchronous direction. The transformed components are labelled as x' and y' in Figs. 12–13. The accomplishment of the rotational transformation is that the 5 and –7th harmonic (as seen from the stationary reference frame) are now seen as the 6 and –6th, and can be both controlled by a single resonant VPI controller placed in each axes. The controller should be tuned for the 6th harmonic ($h = 6$).

In the case of a five-phase system dominant low-order harmonics that map into the second plane are –3, 7, –13 and 17th. The rotation of the x'–y' plane should now be in the synchronous direction at twice the synchronous speed. The harmonics will then be seen in the x'–y' plane as the –5, 5, –15 and 15th. Thus, yet again, they can be conveniently controlled with only two pairs of resonant VPI controllers placed in each axes and tuned for the 5 and 15th harmonic ($h = 5$ and $h = 15$).

Finally, in the case of a symmetrical six-phase system all low-order harmonics map into the first plane. Hence the control of the components from the second plane is not required.

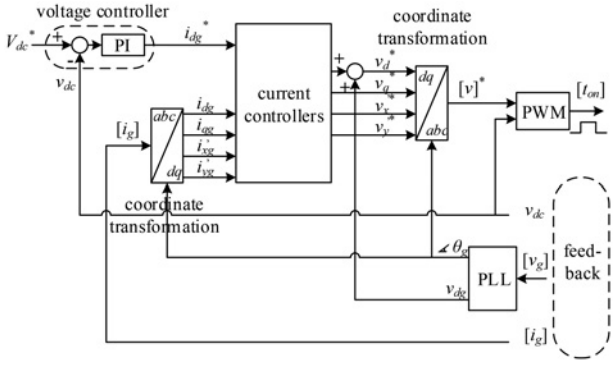

Fig. 12 *Control algorithm for the circuits shown in Fig. 11*

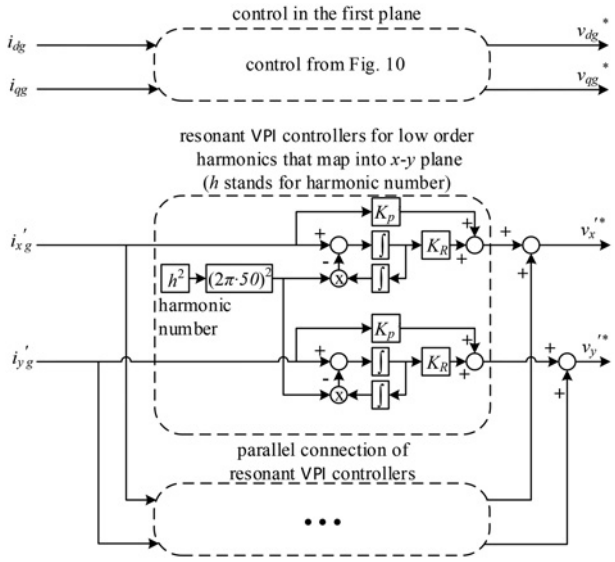

Fig. 13 *Structure of the 'Current controllers' block in Fig. 12*

IET Electr. Power Appl., 2016, Vol. 10, Iss. 3, pp. 217–229

Table 6 Summary of the current controller structures for topologies supplied from a multiphase voltage supply

	Without field generation in the rotor		With pulsating field in the rotor
	(Fig. 5*a*)	(Fig. 5*b*)	(Fig. 6)
Balanced system (equal per-phase filter parameters)	yes	yes	no
Dominant low-order (dead-time induced) harmonics	5, −7, −11 and 13th	−3, 7, −9, 11 and −13th	−5, 7, −11 and 13th
Dominant harmonics that map into the first (α–β) plane	−11 and 13th	−9 and 11th	−5, 7, −11 and 13th
Dominant harmonics that map into the second (x–y) plane	5 and −7th	−3, 7 and −13th	none
Number of PI controller pairs	single controller pair	single controller pair	single controller pair
Number of resonant VPI controller pairs in the α–β plane and their tuning (h)	single controller pair $h = 12$	single controller pair $h = 10$	three controller pairs $h = 2$, 6 and 12
Number of resonant VPI controller pairs in the x'–y' plane and their tuning (h)	single controller pair $h = 6$	two controller pairs $h = 5$ and 15	no controllers

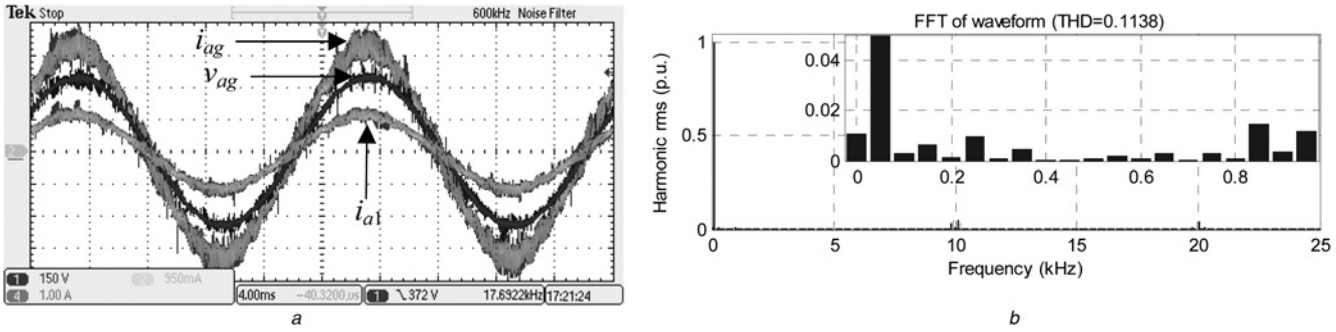

Fig. 14 *Example of the charging performance of the topology of Fig. 2*

a Grid phase voltage v_{ag}, grid current i_{ag}, and machine current i_{a1}
b Spectrum of grid current i_{ag}. Results taken from [23]

It should be noted that all control algorithms of this section are also valid for vehicle-to-grid (V2G) operation. The only difference is that a minus sign should be placed in front of the reference for the grid current d-component i_{dg}^{*} in Figs. 9 and 12.

Current controller structures for the topologies discussed in this section are summarised in Table 6.

4 Experimental results

4.1 Charging from a three-phase grid (Figs. 2–3)

In this section experimental performance that can be obtained with topologies elaborated in Section 2.2 is addressed.

In Fig. 14 an example of the charging performance of the topology of Fig. 2 is given. As can be seen, grid current i_{ag} is sinusoidal and in phase with the grid phase voltage v_{ag}, demonstrating operation with unity power factor. Fig. 14*b* shows grid current spectrum, and it is obvious that control is capable of suppressing low-order harmonics, which are all below 1% of the fundamental. Machine current i_{a_1} is also shown in Fig. 14*a*. It has identical shape as the grid current, however it is three times lower. This is a consequence of the fact that three machine phases are connected to each grid phase; thus each machine phase carries one third of the grid current i_{ag} (Table 1). In this topology there is no field production in the machine rotor (Fig. 4*a*); hence all three grid phases naturally have equal fundamental harmonic values.

An example of a topology that has a field production in the rotor during the charging process is given in Fig. 15, for the case of the topology shown in Fig. 3*b*. As shown by (6), this topology has unequal filter parameters of the equivalent scheme (Fig. 8). Nevertheless, it can be seen that all three grid currents have equal fundamental harmonic values. This is a consequence of the proper operation of the control part that is in charge of unbalance control (Table 5), that is, the suppression of the grid current fundamental component that rotates in the anti-synchronous direction. The presence of the filter parameter unbalance is only obvious from switching ripples of grid currents, as they are not equal among the three phases. As in Fig. 14, the grid currents are in phase with grid phase voltages; thus unity power factor operation is obtained. From Fig. 15*b* it can be seen that grid current is of excellent quality.

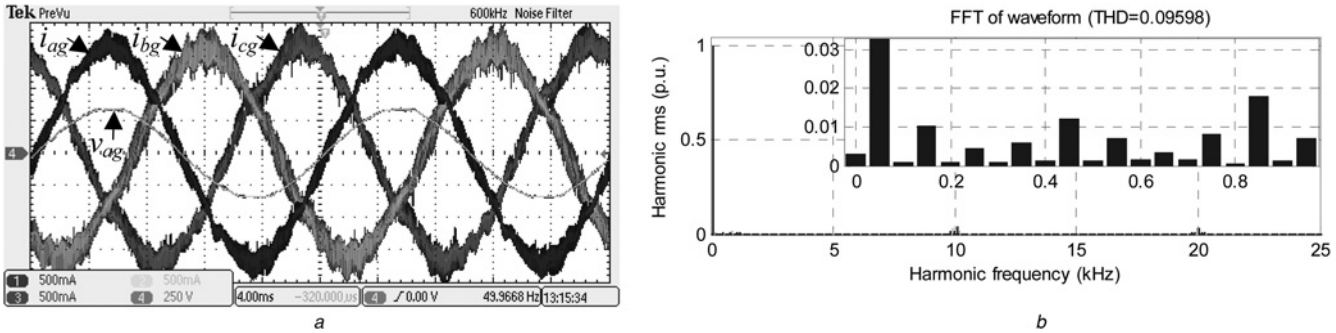

Fig. 15 *Example of a topology Fig. 3b that has a field production in the rotor during the charging process*

a Grid phase voltage v_{ag}, and grid currents i_{ag}, i_{bg} and i_{cg}
b Spectrum of grid current i_{ag}. Results taken from [25]

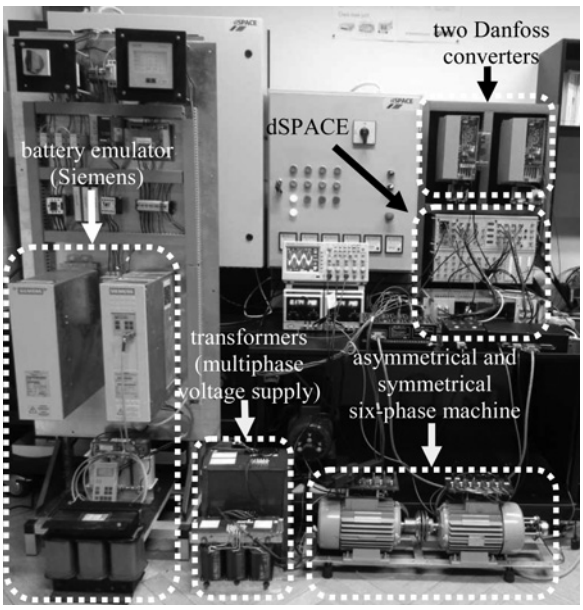

Fig. 16 *Experimental rig*

Experimental setups, used to generate the results in Figs. 14–15, are described in [23, 25], respectively.

4.2 Charging from a multiphase voltage source (Figs. 5–6)

Topologies of Figs. 5*a* and 6 have been evaluated experimentally in [30]. To further support and reconfirm theoretical analysis in Section 2.3 and control algorithms of Section 3.2, a new set of experiments are performed using similar machines and converters.

This experimental rig is shown in Fig. 16. To obtain isolation and asymmetrical six-phase voltage supply, two transformers with connected primary windings are utilised, as in [30]. Symmetrical six-phase voltage set is obtained also as in [30], from a single transformer that has all six terminals of the secondary accessible (without a neutral point on the secondary). A Siemens converter is utilised to emulate a battery and an optional dc–dc converter (right-hand side part of Fig. 1*d*). Two three-phase Danfoss converters with connected dc-buses are utilised as a six-phase converter (left-hand side of Fig. 1*d*). A resistor of a value of 0.5 Ω is placed between the Siemens converter and the Danfoss converters to emulate battery's internal resistance. Experimental rig data can be found in Appendix 2 and further details are available in [35].

For the topology of Fig. 5*a*, dc-bus voltage is set to 700 V. The reference for the *d*-component of the grid current is set to the value $i_{dg}^{*} = 2.5$ A for the charging mode and to $i_{dg}^{*} = -2.5$ A for the V2G mode. Experimental results are shown in Figs. 17 and 18 for the charging and V2G mode, respectively. From Fig. 17 it can be seen that machine currents are in phase with voltages of the asymmetrical six-phase supply; thus, yet again a unity power factor is achieved. However, machine current i_{c1} is in phase with voltage v_{b1}. This is a consequence of the phase transposition in Fig. 5*a*, as Table 3 clearly states that in this topology grid current i_{b1g} and machine current i_{c1} are the same current. Spectrum of machine current i_{a1} is shown in Fig. 17*b*, and it demonstrates excellent current quality. Low-order harmonics are below 1% of the fundamental, which validates proposed control algorithms and current control structure given in Table 6. As in this topology a field is not produced in machine's rotor, currents naturally do not contain any unbalance. Indeed, in Fig. 17*a* the two currents have very similar waveforms.

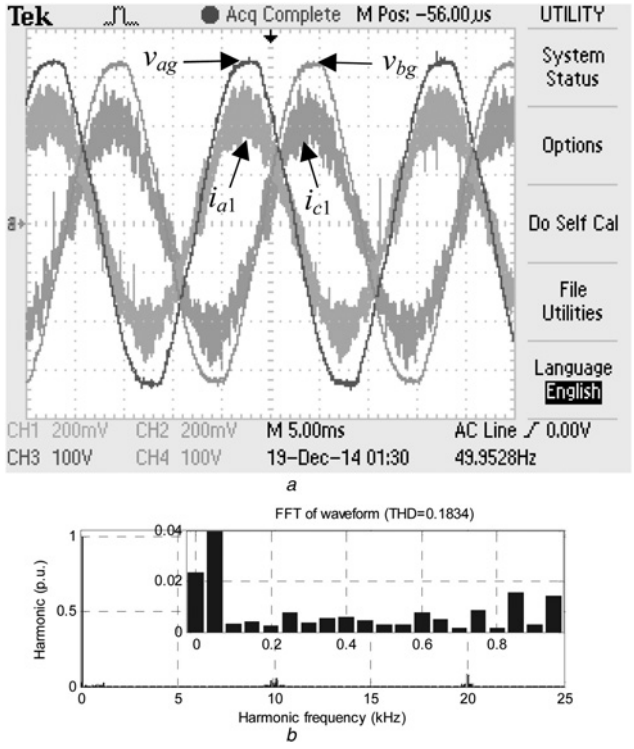

Fig. 17 *Charging mode*

a Grid phase voltages v_{ag}, v_{bg} and machine currents i_{a1} and i_{c1}
b Spectrum of machine current i_{a1}

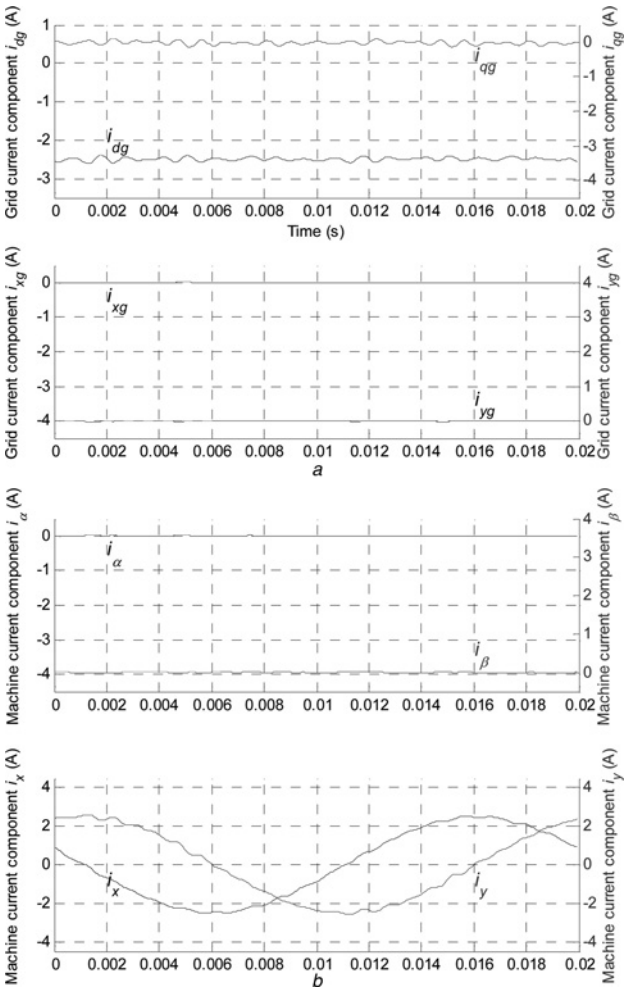

Fig. 18 *V2G mode*

a Grid current components
b Machine current components – excitation mapping into the two machine's planes

IET Electr. Power Appl., 2016, Vol. 10, Iss. 3, pp. 217–229

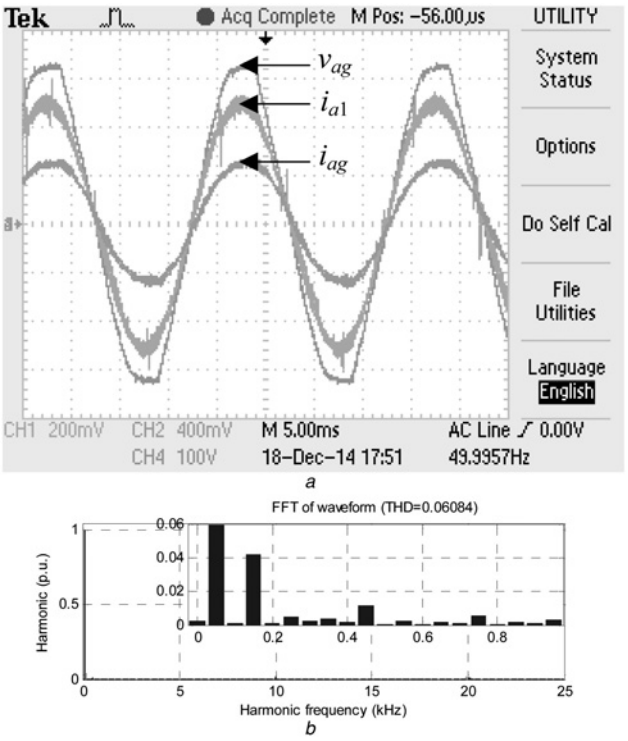

Fig. 19 *Charging mode*

a Grid phase voltage v_{ag}, grid current i_{ag} and machine current i_{a1}
b Spectrum of grid current i_{ag}

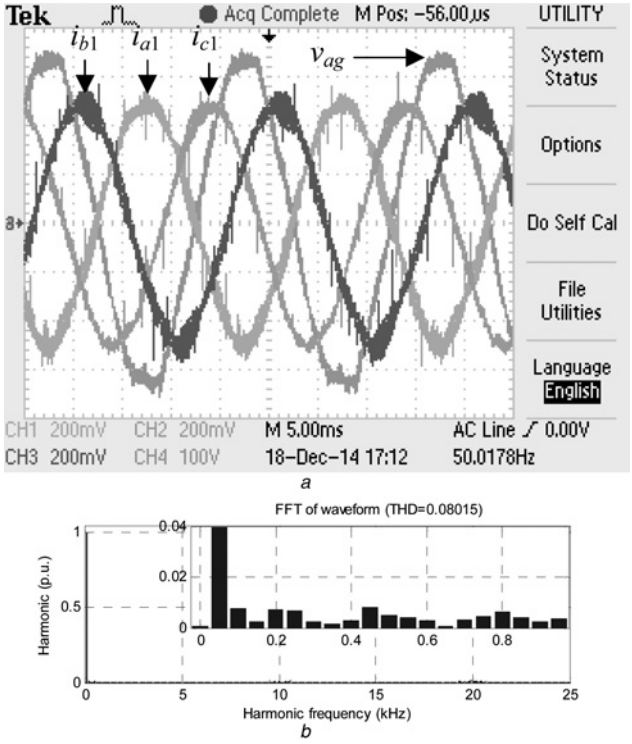

Fig. 20 *V2G mode*

a Grid phase voltage v_{ag}, and machine currents i_{a1}, i_{c1} and i_{b1}
b Spectrum of machine current i_{a1}

Fig. 18 is given for V2G operation and is created using experimental data retrieved from the dSPACE system. From Fig. 18*a* it can be seen that the grid current *d*-component is controlled to its reference ($i^*_{dg} = -2.5$ A). The remaining three current components are completely supressed by control. As the *q*-component is kept at zero, unity power factor operation is again verified. As already stated in Section 2, to assess if a torque is produced during charging/V2G process, machine current components should be observed in a decoupled domain. For V2G operation they are shown in Fig. 18*b*. Obviously there is no excitation in the torque producing (α–β) plane. As predicted by theoretical analysis (Fig. 7*b*), the whole excitation is transferred into the second (non-torque producing) plane. Thus, a torque-free operation is verified, and the machine does not have to be mechanically locked during the charging/V2G operation.

Experimental results for the topology of Fig. 6 are given in Figs. 19–20. The symmetrical six-phase voltage source is obtained as in [30], from a single conventional transformer, rather than from a transformer with two secondary windings, as in [28]. Therefore, the control is slightly different than the one described in Section 3, mainly due to the requirement for zero-sequence current control (the difference is minor and is beyond the scope). In [30] it is shown that the topology can operate with reduced dc-bus voltage, which is verified here. The dc-bus voltage is set to 550 V. References for grid current *d*-component i^*_{dg} are set to 2A and –2A for charging and V2G mode, respectively.

In Fig. 19*a* grid current i_{ag} before the transformer and machine current i_{a1} are shown together with the grid phase voltage. A unity power factor operation is obvious. It can be seen that the two currents are very similar (the oscilloscope channel settings are different). From Fig. 19*b* it can be seen that the grid current i_{ag} contains the 3rd harmonic, which is also noted in [30]. This harmonic is not introduced by inverter dead-time, as it exists even when there is no load at the transformer's secondary. Its existence is due to the saturation and the grounding of the neutral point of the transformer primary. The remaining low-order harmonics have very low values.

V2G operation is demonstrated in Fig. 20. All three currents of the first machine set are shown. At first, it is obvious that the machine current i_{a1} is in phase opposition with the voltage; thus unity power factor is achieved in this mode as well. As in topologies of Fig. 3, there is pulsating field production in the machine's rotor during the charging/V2G operation. Therefore, as explained in Section 3, filter parameters of the equivalent scheme again do not have the same values. However, it is obvious that control (Table 6) manages to suppress the unbalance. Thus all three currents in Fig. 20*a* have the same fundamental harmonic values. Spectrum of the machine current i_{a1} is shown in Fig. 20*b*. As in [30] it does not contain the third harmonic. Moreover, all low-order harmonics have very low values (below 1% of the fundamental), which again verifies the current control structure given in Table 6.

It should be noted that encoders were utilised in both topologies discussed in this section to continuously monitor speed of machines' rotors during the charging and V2G operation. They showed no movement, which again verifies torque-free operation. As these results are completely flat lines at exactly zero value, authors chose not to include them in the paper.

On the basis of the experimental results in Figs. 14, 15 and 17–20 it can be concluded that unity power factor and excellent current quality (very small values of low-order harmonics) can be obtained with all topologies. As a torque is not produced in any of the topologies, the only notable difference in charging/V2G performance is switching ripple of the currents. As it is highly dependent on filter parameters, it has different values in all discussed topologies.

5 Conclusions

The paper provides an overview of the fast on-board integrated chargers for EVs based on multiphase systems. All discussed topologies incorporate a multiphase machine and a multiphase inverter into the charging/V2G process to make savings in the cost, weight and space in the vehicle. For each topology operating principles are explained. The control is elaborated in detail for both charging and V2G mode. Finally, the validity of theoretical

considerations and control algorithms for some of the discussed charging solutions is illustrated using experimental results and experimental performance of all discussed topologies is compared.

The solutions covered by the paper encompass five-, six-, and nine-phase topologies. However, an extension to higher phase numbers is straightforward and, as the phase number increases, there are more and more options available. The idea used for the fast three-phase charging in conjunction with a five-phase system can be extended in a simple manner to all multiphase systems with a prime phase number. If a machine has more than three three-phase windings, the solution discussed in conjunction with a nine-phase machine is directly applicable by using grid connection to just three neutral points. Alternatively, in say, an eighteen-phase system with six isolated neutral points, it also becomes possible to connect each grid phase simultaneously to two neutral points. This would decrease the equivalent filtering inductance since in effect six machine phases would be paralleled to one grid phase, but would keep all machine's phases in operation during charging thus preserving the full charging power. The opportunities for full on-board battery charger integration, offered by multiphase machines and power electronics are thus vast. Needless to say, two-level multiphase converter can be replaced with a multilevel multiphase converter with no impact on the operating principles.

6 Acknowledgment

The authors acknowledge the Engineering and Physical Sciences Research Council (EPSRC), U.K., and the Provincial Secretariat for Science and Technological Development of AP Vojvodina, Republic of Serbia, for supporting, respectively, the 'Vehicle Electrical Systems Integration (VESI)' project (EP/I038543/1) and 'Research and Development of Energy Efficient Power Supply and Propulsion Systems of Electric Vehicles' project (contract no. 114-451-2248/2011-03).

7 References

1 Yilmaz, M., Krein, P.T.: 'Review of battery charger topologies, charging power levels, and infrastructure for plug-in electric and hybrid vehicles', *IEEE Trans. Power Electron.*, 2013, **28**, (5), pp. 2151–2169
2 Yilmaz, M., Krein, P.T.: 'Electrification of the transportation system'. MIT Energy Initiative Symp., 2010, http://mitei.mit.edu/publications/reports-studies/electrification-transportation-system (full report)
3 Wu, H.H., Gilchrist, A., Sealy, K., *et al.*: 'A review on inductive charging for electric vehicles'. Proc. IEEE Int. Electric Machines and Drives Conf. IEMDC, 2011, pp. 143–147
4 Ching, T.W., Wong, Y.S.: 'Review of wireless charging technologies for electric vehicles'. Proc. Int. Conf. on Power Electronics Systems and Applications PESA, 2013, pp. 1–4
5 Khaligh, A., Dusmez, S.: 'Comprehensive topological analysis of conductive and inductive charging solutions for plug-in electric vehicles', *IEEE Trans. Veh. Technol.*, 2012, **61**, (8), pp. 3475–3489
6 Yilmaz, M., Krein, P.T.: 'Review of integrated charging methods for plug-in electric and hybrid vehicles'. Proc. IEEE Int. Conf. on Vehicular Electronics and Safety ICVES, 2012, pp. 346–351
7 Sakr, N., Sadarnac, D., Gascher, A.: 'A review of on-board integrated chargers for electric vehicles'. Proc. European Power Electronics and Applications Conf. EPE-ECCE, 2014, pp. 1–10
8 Zaja, M., Oprea, M., Suarez, C.G., *et al.*: 'Electric vehicle battery charging algorithm using PMSM windings and an inverter as an active rectifier'. Proc. IEEE Vehicle Power and Propulsion Conf. VPPC, 2014, pp. 1–6
9 Haghbin, S., Lundmark, S., Alakula, M., *et al.*: 'Grid-connected integrated battery chargers in vehicle applications: review and new solution', *IEEE Trans. Ind. Electron.*, 2013, **60**, (2), pp. 459–473
10 Cocconi, A.: 'Combined motor drive and battery recharge system'. US Patent No. US 5,341,075, 1994
11 Lacressonniere, F., Cassoret, B.: 'Converter used as a battery charger and a motor speed controller in an industrial truck'. Proc. European Power Electronics and Applications Conf. EPE, 2005, pp. 1–7
12 Santiago, J.D., Bernhoff, H., Ekergard, B., *et al.*: 'Electrical motor drivelines in commercial all-electric vehicles: A review', *IEEE Trans. Veh. Technol.*, 2012, **61**, (2), pp. 475–484
13 Dupuy, P.: 'Electric traction chain for an automobile'. US Patent No. US 2011/0187185 A1, 2011
14 Renault press kit: 'Renault ZOE: the electric supermini for everyday use', 26 February 2013, www.media.renault.com
15 Briane, B., Loudot, S.: 'Rapid reversible charging device for an electric vehicle'. US Patent No. US 2011/0254494 A1, 2011
16 Loudot, S., Briane, B., Ploix, O., *et al.*: 'Fast charging device for an electric vehicle'. US Patent No. US 2012/0286740 A1, 2013
17 Hong, J., Lee, H., Nam, K.: 'Charging method for the secondary battery in dual-inverter drive systems for electric vehicles', *IEEE Trans. Power Electron.*, 2015, **30**, (2), pp. 909–921
18 Su, G.J.: 'Electric vehicle system for charging and supplying electrical power'. US Patent No. US 7,733,039 B2, 2010
19 Subotic, I., Jones, M., Levi, E.: 'A fast on-board integrated battery charger for four-motor EVs'. Proc. Int. Conf. on Electrical Machines ICEM, 2014, pp. 2066–2072
20 De Sousa, L., Silvestre, B., Bouchez, B.: 'A combined multiphase electric drive and fast battery charger for electric vehicles'. Proc. IEEE Vehicle Power and Propulsion Conf. VPPC, 2010, pp. 1–6
21 De Sousa, L., Bouchez, B.: 'Combined electric device for powering and charging'. US patent No. US 2011/0221363 A1, 2011
22 Haghbin, S., Guillen, I.S.: 'Integrated motor drive and non-isolated battery charger based on the torque cancelation in the motor'. Proc. IEEE Int. Conf. on Power Electronics and Drive Systems PEDS, 2013, pp. 824–829
23 Subotic, I., Bodo, N., Levi, E., *et al.*: 'On-board integrated battery charger for EVs using an asymmetrical nine-phase machine', *IEEE Trans. Ind. Electron.*, 2015, **62**, (5), pp. 3285–3295
24 Subotic, I., Levi, E., Bodo, N.: 'A fast on-board integrated battery charger for EVs using an asymmetrical six-phase machine'. Proc. IEEE Vehicle Power and Propulsion Conf. VPPC, 2014, pp. 1–6
25 Subotic, I., Bodo, N., Levi, E.: 'An EV drive-train with integrated fast charging capability', *IEEE Trans. Power Electron.*, 2015, **31**, (2), pp. 1461–1471
26 Subotic, I., Levi, E., Jones, M., *et al.*: 'An integrated battery charger for EVs based on an asymmetrical six-phase machine'. Proc. IEEE Industrial Electronics Society Conf. IECON, 2013, pp. 7242–7247
27 Subotic, I., Levi, E., Jones, M., *et al.*: 'Multiphase integrated on-board battery chargers for electrical vehicles'. Proc. European Power Electronics and Applications Conf. EPE-ECCE, 2013, pp. 1–10
28 Subotic, I., Levi, E.: 'An integrated battery charger for EVs based on a symmetrical six-phase machine'. Proc. IEEE Int. Symp. on Industrial Electronics ISIE, 2014, pp. 2074–2079
29 Levi, E., Bojoi, R., Profumo, F., *et al.*: 'Multiphase induction motor drives – a technology status review', *IET Electric Power Appl.*, 2007, **1**, (4), pp. 489–516
30 Subotic, I., Bodo, N., Levi, E., *et al.*: 'Isolated chargers for EVs incorporating six-phase machines', *IEEE Trans. Ind. Electron.*, doi: 10.1109/TIE.2015.2412516
31 Levi, E., Jones, M., Vukosavic, S.N., *et al.*: 'A novel concept of a multiphase, multimotor vector controlled drive system supplied from a single voltage source inverter', *IEEE Trans. Power Electron.*, 2004, **19**, (2), pp. 320–335
32 Dusmez, S., Cook, A., Khaligh, A.: 'Comprehensive analysis of high quality power converters for level 3 off-board chargers'. Proc. IEEE Vehicle Power and Propulsion Conf. VPPC, 2011, pp. 1–10
33 Limongi, L.R., Bojoi, R., Pica, C., *et al.*: 'Analysis and comparison of phase locked loop techniques for grid utility applications'. Proc. Power Conversion Conf. PCC, 2007, pp. 674–681
34 Iqbal, A., Levi, E., Jones, M., *et al.*: 'Generalised sinusoidal PWM with harmonic injection for multi-phase VSIs'. Proc. IEEE Power Electronics Spec. Conf. PESC, 2006, pp. 2871–2877
35 Dumnic, B., Milicevic, D., Popadic, B., *et al.*: 'Advanced laboratory setup for control of electrical drives as an educational and developmental tool'. Proc. IEEE EuroCon, Zagreb, Croatia, 2013, pp. 903–909

8 Appendices

8.1 Appendix 1: derivation of equations in Section 2

All equations in Tables 2 and 4 are obtained using similar derivations. Here the derivation procedure is demonstrated only for the case of the topology shown in Fig. 3*b*.

For derivations it is beneficial to represent a multiphase decoupling matrix in space vector form. In five-phase system it is governed with

$$\underline{i}_{\alpha\beta} = i_\alpha + \mathrm{j}i_\beta = \sqrt{2/5}\left(i_a + \underline{a}i_b + \underline{a}^2 i_c + \underline{a}^3 i_d + \underline{a}^4 i_e\right) \quad (7)$$

$$\underline{i}_{xy} = i_x + \mathrm{j}i_y = \sqrt{2/5}\left(i_a + \underline{a}^2 i_b + \underline{a}^4 i_c + \underline{a}^6 i_d + \underline{a}^8 i_e\right) \quad (8)$$

where $\underline{a} = \exp(j\delta) = \cos\delta + j\sin\delta$ and $\delta = 2\pi/5$.

Grid currents are given with (1), while the correlation between machine and grid currents (Table 1) is governed with

$$i_a = i_{ag} \quad i_b = i_e = i_{bg}/2 \quad i_c = i_d = i_{cg}/2 \quad (9)$$

Substitution of (9) and (1) into (7) leads to the following expression

$$\underline{i}_{\alpha\beta} = \sqrt{\frac{2}{5}} \cdot I \cdot \sqrt{2} \cdot \frac{1}{2} \left\{ \begin{array}{l} \left(e^{j\omega t} + e^{-j\omega t}\right) + \frac{1}{2}\left(e^{j(\omega t-(2\pi/3))} + e^{-j(\omega t-(2\pi/3))}\right) \\ \left(e^{j\delta} + e^{j4\delta}\right) + \frac{1}{2}\left(e^{j(\omega t-(4\pi/3))} + e^{-j(\omega t-(4\pi/3))}\right)\left(e^{j2\delta} + e^{j3\delta}\right) \end{array} \right\} \quad (10)$$

Components that are multiplied by $e^{j\omega t}$ and those multiplied by $e^{-j\omega t}$ can be separated, after which the following expressions are obtained

$$\underline{i}_{\alpha\beta} = \frac{I}{\sqrt{5}} \left\{ e^{j\omega t} \cdot \left[1 + \frac{1}{2}e^{-j(2\pi/3)}\left(e^{j\delta} + e^{j4\delta}\right) + \frac{1}{2}e^{-j(4\pi/3)}\left(e^{j2\delta} + e^{j3\delta}\right)\right] + e^{-j\omega t} \cdot \left[1 + \frac{1}{2}e^{j(2\pi/3)}\left(e^{j\delta} + e^{j4\delta}\right) + \frac{1}{2}e^{j(4\pi/3)}\left(e^{j2\delta} + e^{j3\delta}\right)\right]\right\} \quad (11)$$

$$\underline{i}_{\alpha\beta} = \frac{I}{\sqrt{5}}[e^{j\omega t} \cdot (1.25 - j \cdot 0.9682) + e^{-j\omega t} \cdot (1.25 + j \cdot 0.9682)] \quad (12)$$

$$\underline{i}_{\alpha\beta} = \frac{I}{\sqrt{5}} 1.5811 \cdot [e^{j\omega t} \cdot (0.7906 - j \cdot 0.6124) + e^{-j\omega t} \cdot (0.7906 + j \cdot 0.6124)] \quad (13)$$

$$\underline{i}_{\alpha\beta} = \frac{1.5811}{\sqrt{5}} I \cdot [e^{j\omega t} \cdot e^{-j0.6590} + e^{-j\omega t} \cdot e^{j0.6590}] \quad (14)$$

$$\underline{i}_{\alpha\beta} = \frac{1.5811}{\sqrt{5}} I \cdot [e^{j(\omega t-0.6590)} + e^{-j(\omega t-0.6590)}] = \sqrt{2} \cdot I \cdot \cos(\omega t - 0.659) \quad (15)$$

As can be seen, the expression of the first plane excitation, given in Table 2, is obtained. In a similar manner the excitation in the x–y plane can be determined, as well as excitations in all the other considered topologies.

8.2 Appendix 2: experimental rig data

Dc source/sink (battery emulator): Siements Simovert AFE 6SE7021-3EB81-Z.

Controller: dSPACE containing DS1006 processor board, DS5101 digital waveform output board, DS2004 A/D board and DS3001 incremental encoder board.

Converter: Two Danfoss FC302 converters with connected dc-buses. Interface and protection card is added to converters to allow a higher degree of controllability.

Asymmetrical six-phase IM: the parameters are $R_s = 12.8\ \Omega$, $R_r = 10.5\ \Omega$, $L_m = 600$ mH, $L_{\gamma s} = L_{\gamma r} = 37.6$ mH. Obtained by rewinding a 380 V, 50 Hz, 1.1 kW three-phase machine.

Symmetrical six-phase IM: the parameters are $R_s = 14.7\ \Omega$, $R_r = 11.8\ \Omega$, $L_m = 612$ mH, $L_{\gamma s} = L_{\gamma r} = 39.5$ mH. Obtained by rewinding a 380 V, 50 Hz, 1.1 kW three-phase machine.